

Effect of Initial Membrane Water Content on the Cold Start Performance of PEMFC

Zhenwei Wang, Binbin Sun, Di Huang, Tianqi Gu, Zhenhao Liu

Abstract—Aiming at the problem of start-up failure caused by icing during the cold start of proton exchange membrane fuel cell, COMSOL Multiphysics software is used to establish a cold start transient model of three-dimensional multiphase flow with multi-physics field coupling for proton exchange membrane fuel cell. Through the cold-start model simulation, the effects of the initial membrane water content on the current density, icing rate, temperature and other characteristics of the battery cold-start are investigated. The numerical results show that the higher the initial water content, the greater the initial current density and a faster temperature rises. However, it is accompanied by a larger icing rate and earlier icing time, which leads to a faster decline in battery performance. Lower initial water content is helpful to delay icing, and the battery temperature rises higher, which is more beneficial to cold start.

Index Terms—PEMFC, initial membrane water, cold start, multiphase coupling

I. INTRODUCTION

PROTON exchange membrane fuel cell (PEMFC), which directly convert chemical energy into electrical energy, are celebrated for their zero emissions and high energy density, making them ideal for future onboard energy systems [1,2]. However, the challenge of internal icing during cold starts at sub-zero temperatures remains a significant obstacle. This icing occurs when water produced in the cathode catalytic layer (CL) freezes, leading to pore blockage and hindering electrochemical reactions. If the temperature remains below 0°C, the electrochemical reactions stop, resulting in a failed cold start. Furthermore,

Manuscript received September 26, 2023; revised May 17, 2024. This work was supported in part by the Major Innovation Projects in Shandong under Grant 2020CXGC010405 and 2020CXGC010406, the Innovation team project of "Qing-Chuang science and technology plan" of colleges and universities in Shandong Province 2021KJ083, the National Natural Science Foundation Project of China under Grant 52102465, the Postdoctoral Science Foundation of China and Shandong under Grant 2020M680091 and 202003042.

Zhenwei Wang is a graduate of School of Transportation and Vehicle Engineering, Shandong University of Technology, Zibo, 255000 PR China. (e-mail: zhenweiwang2022@163.com).

Binbin Sun is a professor of School of Transportation and Vehicle Engineering, Shandong University of Technology, Zibo, 255000 PR China. (corresponding author to provide phone: 86-13708941464; e-mail: sunbin_sdut@126.com).

Di Huang is a graduate student of School of Transportation and Vehicle Engineering, Shandong University of Technology, Zibo, 255000 PR China. (e-mail: huangdi934675559@163.com).

Tianqi Gu is a graduate student of School of Transportation and Vehicle Engineering, Shandong University of Technology, Zibo, 255000 PR China. (e-mail: tianqi.gu@outlook.com).

Zhenhao Liu is a graduate student of School of Transportation and Vehicle Engineering, Shandong University of Technology, Zibo, 255000 PR China. (e-mail: 15163095630@163.com).

the expansion of water into ice can cause substantial damage to the membrane electrode structure [3,4].

A significant body of research has focused on understanding the low-temperature startup characteristics and internal icing mechanisms of proton exchange membrane fuel cells. The team led by Pu He developed a one-dimensional multiphase non-isothermal unsteady-state cold start model to explore the impact of platinum loading in the cathode CL on startup performance, finding that increased platinum loading delays initial ice formation and reduces icing rates [5]. Jie Zhao created a one-dimensional transient multi-physical field coupling model to analyze the effects of constant voltage and constant current outputs on PEMFC cold starts [6]. Hosseini utilized a two-dimensional CFD model to examine how stoichiometric coefficients and the amount of saturated water in the cathode gas diffusion layer (GDL) influence its performance [7]. Despite these advancements, one-dimensional and two-dimensional models often rely on assumptions and simplifications that fail to capture the full spatial distribution of physical quantities within the cell. To address this, Peng Xu developed a three-dimensional numerical model of a fuel cell single cell for cold starts, introducing the Water Storage Capacity (WSC) index as a predictor of cold start performance—higher WSC values correlate with better performance [8]. Lei Yao established a three-dimensional transient multiphase flow mathematical model, suggesting that increasing the volume fraction of ionic polymer in the cathode CL could improve the utilization efficiency of the water storage space [9]. Additional studies include Wei's examination of the cooling cycle system's role during low-temperature startups [10], Liao's research on the effect of gas channel structure on startup performance [11], and Yang's modeling of the dynamics of the cold start process, which demonstrated that increasing the cathode CL thickness provides more ohmic heat, aiding temperature rise and preventing localized icing [12]. Ko explored the impact of metal bipolar plates versus graphite plates, noting that metal plates, with their superior heat transfer properties, allow for quicker heating and thus better cold start performance [13].

This paper presents a three-dimensional multiphase flow multi-physics field-coupled proton exchange membrane fuel cell cold-start model. It comprehensively incorporates water transfer and phase transition processes, gas-liquid two-phase flow, electrochemical reactions, and ion and electron transport with heat transfer inside the cell. We analyze the impact of various initial membrane water contents on the current density, ice volume fraction, and temperature of the fuel cell.

II. PEMFC COLD START NUMERICAL MODEL

In this study, we have developed a three-dimensional multiphase flow multi-physical field-coupled model for the cold start of a proton exchange membrane fuel cell (PEMFC). To optimize the use of computing resources, the geometric model employed is a single-channel PEMFC with dimensions of $3.47\text{mm} \times 2\text{mm} \times 20\text{mm}$. The structure of the model, depicted in Figure 1, is composed sequentially from top to bottom of the anode plate, anode side gas flow channel, anode diffusion layer, anode catalytic layer, proton exchange membrane, cathode catalytic layer, cathode diffusion layer, cathode side gas flow channel, and cathode plate.

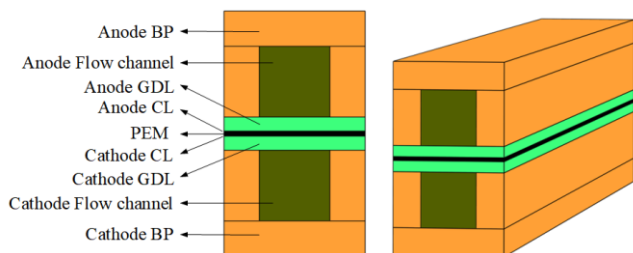


Fig. 1 Geometric model of PEMFC

PEMFC operation encompasses complex processes such as material transfer, hydrodynamics, electrochemistry, heat transfer, and phase transitions. Accurate simulation of these processes within the fuel cell stack requires careful selection of relevant parameters. The parameters for each physical field in the model are detailed in TABLE I.

 TABLE I
 GEOMETRIC AND PHYSICAL PARAMETERS OF PEMFC MODEL

Parameter name	value
Proton exchange membrane thickness (Nafion 112)	0.05 mm
Membrane equivalent mass; density	1100 g/mol; 1980 kg·m ⁻³
Thickness of CL	0.01 mm
Thickness of GDL	0.2 mm
Channel length; width; depth; rib width	20; 1; 1; 1 mm
Porosity of CL; GDL	0.3; 0.6
Volume fraction of ionomer in CL	0.25
Electrical conductivities of CL; GDL; BP	300; 300; 20000 S·m ⁻¹
Thermal conductivities of membrane; CL; GDL; BP	0.95; 1; 1; 20 W m ⁻¹ ·K ⁻¹
Specific heat capacities of membrane; CL; GDL; BP	833; 3300; 568; 1580 J·kg ⁻¹ ·K ⁻¹
Intrinsic permeabilities of CL; GDL	6.2×10^{-13} ; 6.2×10^{-12} m ²
Cell voltage	0.7 V
Stoichiometric ratio of anode; cathode	2.0; 2.0
Relative humidities of inlet gases	0
Density of liquid water; ice	990; 920 kg·m ⁻³
Specific heat capacity of hydrogen; oxygen; water vapor; liquid water; ice	14283; 919; 2014; 4182; 2060 J·kg ⁻¹ ·K ⁻¹
Temperature of inlet gas; environment	-20°C; -20°C

A. Model Assumptions

The construction and calculation of PEMFC cold start model include the following assumptions:

(1) Fluid Dynamics: The fluid inside the fuel cell is considered as incompressible laminar flow.

(2) Gas Properties: The reaction gases are treated as ideal gases.

(3) Gas Transport: No reaction gases are transported through the proton exchange membrane (PEM).

(4) Structural Integrity: Structural deformations and the effects of gravity inside the battery are neglected.

(5) Material Properties: The proton exchange membrane (PEM), catalytic layers (CL), and gas diffusion layers (GDL) are assumed to be isotropic, meaning they have uniform properties in all directions.

(6) Permeability: Gases such as hydrogen and oxygen are assumed not to permeate the PEM.

(7) Humidity Conditions: Intake air is assumed to be non-humidified, and water vapor is immediately carried away in the runners.

B. PEMFC Cold Start Control Equation

The control equations of proton exchange membrane fuel cell cold start mainly include mass, momentum, energy, composition and charge conservation equations. The specific expressions of each equation are as follows.

Mass conservation equation of mixed gas phase:

$$\frac{\partial}{\partial t} (\varepsilon (1 - s_{lq} - s_{ice}) \rho_g) + \nabla \cdot (\rho_g \vec{u}_g) = S_m \quad (1)$$

where, ε is the porosity of CL and GDL, s_{lq} and s_{ice} are the volume fractions of liquid water and ice, respectively; ρ_g is the density of the gas mixture (kg·m⁻³); \vec{u}_g is the velocity vector of the gas mixture (m·s⁻¹); and the mass source term is S_m (kg·m⁻³·s⁻¹), which includes the depletion of hydrogen, oxygen, and the phase transition of water vapor.

Mass conservation equation of non-frozen membrane water content:

$$\frac{\rho_{mem}}{EW} \frac{\partial}{\partial t} (\omega \lambda_{nf}) = \frac{\rho_{mem}}{EW} \nabla \cdot (D_{mw}^{eff} \nabla \lambda_{nf}) + S_{nfm} \quad (2)$$

where, ρ_{mem} is the dry membrane density (g·m⁻³); EW is the equivalent mass of the membrane; λ_{nf} is the content of non-frozen membrane water in the electrolyte, and ω is the electrolyte volume fraction of the catalytic layer; D_{mw}^{eff} is the effective diffusion coefficient of non-frozen membrane water (m²·s⁻¹); the mass source term of non-frozen membrane water is S_{nfm} (kg·m⁻³·s⁻¹), including the formation, phase transition and electroosmotic migration of ionomer water.

Mass conservation equation of frozen membrane water content:

$$\frac{\rho_{mem}}{EW} \frac{\partial}{\partial t} (\omega \lambda_f) = S_{fmw} \quad (3)$$

where, λ_f is the amount of frozen water in the electrolyte; and the mass source term of frozen membrane water is S_{fmw} (kg·m⁻³·s⁻¹), including the source term of non-frozen membrane water to frozen membrane water.

Mass conservation equation of liquid water:

$$\frac{\partial}{\partial t} (\rho_{lq} \varepsilon s_{lq}) = \nabla \cdot (\rho_{lq} D_{lq} \nabla s_{lq}) + S_{lq} \quad (4)$$

where, ρ_{lq} is the density of liquid water (kg·m⁻³·s⁻¹); D_{lq} is the diffusion coefficient of liquid water (m²·s⁻¹); the mass source term of liquid water is S_{lq} (kg·m⁻³·s⁻¹); which includes the phase transition of liquid water.

Mass conservation equation of ice:

$$\frac{\partial}{\partial t}(\rho_{ice} \varepsilon s_{ice}) = S_{ice} \quad (5)$$

where, ρ_{ice} is the density of ice ($\text{kg}\cdot\text{m}^{-3}$); the ice source term is S_{ice} ($\text{kg}\cdot\text{m}^{-3}\cdot\text{s}^{-1}$), which includes the phase transition of ice.

Momentum conservation equation:

$$\begin{aligned} \frac{\partial}{\partial t} \left(\frac{\rho_g \vec{u}_g}{\varepsilon(1-s_{lq}-s_{ice})} \right) + \nabla \cdot \left(\frac{\rho_g \vec{u}_g \vec{u}_g}{\varepsilon^2(1-s_{lq}-s_{ice})^2} \right) = -\nabla p_g \\ + \mu_g \nabla \cdot \left(\nabla \left(\frac{\vec{u}_g}{\varepsilon(1-s_{lq}-s_{ice})} \right) + \nabla \left(\frac{\vec{u}_g^T}{\varepsilon(1-s_{lq}-s_{ice})} \right) \right) \\ - \frac{2}{3} \mu_g \nabla \cdot \left(\nabla \left(\frac{\vec{u}_g}{\varepsilon(1-s_{lq}-s_{ice})} \right) \right) + S_u \end{aligned} \quad (6)$$

where, p_g is the gas phase pressure (Pa); μ_g is the kinetic viscosity of the gas phase ($\text{kg}\cdot\text{m}^{-1}\cdot\text{s}^{-1}$); S_u is the momentum source term of the equation ($\text{kg}\cdot\text{m}^{-3}\cdot\text{s}^{-1}$).

Conservation equation of gas composition:

$$\frac{\partial}{\partial t}(\varepsilon(1-s_{lq}-s_{ice})\rho_g Y_i) + \nabla \cdot (\rho_g \vec{u}_g Y_i) = \nabla \cdot (\rho_g D_i^{eff} \nabla Y_i) + S_i \quad (7)$$

where, the subscript i denotes each gas component; Y_i is the mass fraction of each gas component; D_i^{eff} is the effective diffusion coefficient of the gas; and S_i is the source term of the equation for the gas component, which includes the depletion of hydrogen, oxygen, or the phase transition of water vapor.

Energy conservation equation:

$$\frac{\partial}{\partial t}((\rho C_p)_{fl,sl}^{eff} T) + ((\rho C_p)_{fl}^{eff} \vec{u}_g T) = \nabla \cdot (k_{fl,sl}^{eff} \nabla T) + S_T \quad (8)$$

where, $(\rho C_p)_{fl,sl}^{eff}$ is the effective volume heat capacity ($\text{J}\cdot\text{kg}^{-1}\cdot\text{K}^{-1}$); T is temperature (K); $k_{fl,sl}^{eff}$ is the effective thermal conductivity ($\text{W}\cdot\text{m}^{-1}\cdot\text{K}^{-1}$); S_T is the source term of heat, which mainly includes the reversible heat of electrochemical reaction, the activation heat, the ohmic heat and the latent heat of various phase transitions of water.

Charge conservation equation:

$$-\nabla \cdot (\kappa_{ion}^{eff} \nabla \phi_{ion}) = S_{ion} \quad (9)$$

$$-\nabla \cdot (\kappa_{ele}^{eff} \nabla \phi_{ele}) = S_{ele} \quad (10)$$

where, κ_{ion}^{eff} and κ_{ele}^{eff} are the effective conductivities of ions and electrons, respectively ($\text{s}\cdot\text{m}^{-1}$); ϕ_{ion} and ϕ_{ele} are the ionic and electronic potentials, respectively ($\text{s}\cdot\text{m}^{-1}$); S_{ion} and S_{ele} are ion and electron source terms, respectively ($\text{A}\cdot\text{m}^{-3}$).

C. Boundary Conditions

During PEMFC operation, the consumption of reactants is proportional to the output current. The inlet flow rate of the reaction gas is calculated using the reference current density and the stoichiometric ratio of the cell. The mass flow rates of reactants at the anode and cathode inlets are determined by Equation (11) [14,15].

$$\dot{m}_a = \frac{\rho_g^a \zeta_a I_{ref} A_{act}^a}{2FC_{H_2}} \quad \dot{m}_c = \frac{\rho_g^c \zeta_c I_{ref} A_{act}^c}{2FC_{O_2}} \quad (11)$$

where, ζ is the stoichiometric ratio of the supplied gas, ρ_g is the average density of the supplied gas, A is the reaction area of the membrane electrode of the fuel cell, I_{ref} is the reference current density used for the calculation of the gas flow rate, F is the Faraday's constant, C_{H_2} and C_{O_2} are the anode inlet hydrogen concentration and cathode inlet oxygen concentration, respectively.

Convective heat transfer boundary conditions are applied to both the ends and sides of the cathode and anode in the battery. The rate of heat transfer between the external surface and the surrounding environment is calculated using Equation (12).

$$\dot{Q} = hA_{wall}(T_{surr} - T_{wall}) \quad (12)$$

where, h is the convective heat transfer coefficient of the surface, taken as $50\text{ W}\cdot\text{m}^{-2}\cdot\text{K}^{-1}$, A_{wall} and T_{wall} are the surface area and temperature of the external wall respectively, and T_{surr} is the ambient temperature.

The potential at the external end of the anode side pole plate is defined as the reference zero potential, while the potential at the external end of the cathode side pole plate represents the output voltage. The thermodynamically reversible potential is expressed by the modified Nernst equation (13).

$$E_r = 1.23 - 0.9 \times 10^{-3} (T - T_0) + \frac{RT}{2F} \ln \left(\frac{P_{H_2} P_{O_2}^{0.5}}{P_{H_2O}} \right) \quad (13)$$

where, T and T_0 refer to the actual temperature and reference temperature (298.15K) at the electrochemical reaction site, respectively; R is the universal gas constant; F is the Faraday constant; P_{H_2} , P_{O_2} , and P_{H_2O} are the partial pressures of hydrogen, oxygen, and water vapor in the fuel cell, respectively.

D. Numerical Method

The model described in this paper is constructed and solved using the commercial finite element analysis software, COMSOL. Control equations and the definition of key parameters are customized and modified within the equation view of the corresponding physical field interface. A coupled multi-physical field model is then solved by selecting a separation step and using the PARDISO direct solver. This model operates as a transient calculation model. To enhance the stability of calculation convergence, the backward difference formula is employed for time stepping when solving the partial differential equations of the PEMFC model. The solver uses a free transient solver step size, with the maximum step size limited to 0.1 seconds. The nonlinear Newton iteration method is utilized, and the Jacobian matrix is updated at each iteration to maintain accuracy and prevent error accumulation. The relative tolerance for the transient solver is set at 0.005 to avoid large errors, compared to the default software value of 0.01. All other solver configuration parameters are set to the software's default values.

III. RESULTS ANALYSIS AND DISCUSSION

A. Model Validation

To validate the accuracy of the PEMFC cold start model, two operating conditions were selected: an ambient environment (15°C) and a low-temperature environment (-5°C). The experimentally measured polarization curves of the PEMFC were compared with those obtained from model simulations for verification, as illustrated in Fig. 2. When the PEMFC operates at middle and low current density ranges, the measured values generally align with the simulated values. However, in the high current density range, there is a noticeable deviation between the simulated and measured values. This deviation, which is less than 5%, is attributed to the simplifications and some idealized assumptions made in the model. Despite this, the overall trend of the curves is consistent, indicating that the cold-start model is capable of predicting the performance of the fuel cell during cold starts.

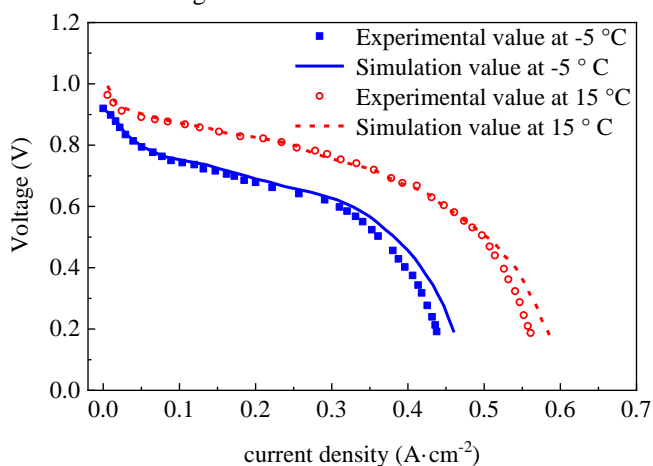


Fig. 2 Model verification: comparison of polarization curves between simulation and experiment

B. Effect Of Initial Membrane Water Content On Current Density

Figure 3 illustrates how the current density varies during the cold start of the fuel cell under different initial membrane state water contents. Specifically, the maximum current densities achieved with initial membrane water contents of 3.6, 5 and 7 were 0.155 A·cm⁻², 0.126 A·cm⁻² and 0.11 A·cm⁻², respectively. This shows that cells with higher initial membrane water contents produce greater current densities. It is believed that a higher water content in the membrane improves the conductivity of the proton exchange membrane, thereby enhancing the current density. The graph also indicates that with an initial membrane water content of 3.6, the current density reaches its peak at around 28 seconds. In contrast, for initial water contents of 7 and 5, the current density quickly reaches its maximum value at the start of the cold start. This suggests that too low a water content can lead to "membrane dryness," which diminishes the membrane's conductivity and hampers the transport of H⁺ ions from the anode to the cathode through the proton exchange membrane. This results in a slower rate of electrochemical reaction, leading to a lower initial current density. As water is generated in the cathode's catalytic layer, concentration diffusion occurs, allowing water to move from the high concentration area at the cathode to the low

concentration area at the anode through the membrane. This process alleviates the "membrane dryness," and the current density gradually increases to its maximum value.

As can be seen in Figure 3, a higher initial membrane water content leads to an earlier decrease in current density. This phenomenon can be attributed to the fact that a higher initial water content not only produces a higher initial current density but also accelerates the rate of water generation. Consequently, the limited water storage capacity of the membrane is quickly exceeded, leading to faster saturation (at approximately -20°C, the saturation value of the membrane water is about 7.3). Once the membrane water content reaches this saturation point, any excess water is converted into ice, which impedes the electrochemical reaction and consequently causes an earlier decrease in current density. Therefore, with initial water contents of 5 and 7, the current density begins to decline earlier. In contrast, an initial membrane water content of 3.6 shows a different behavior; the larger gap between initial and saturated membrane water levels, combined with a slower rate of water production, allows for more extensive water storage. This delays the time it takes to reach the saturation point, resulting in a later drop in current density. Specifically, the current densities for initial membrane state water contents of 3.6, 5, and 7 begin to decline sharply at 20s, 37s, and 63s, respectively, marking the point at which the electrochemical reactions cease and the cold start fails.

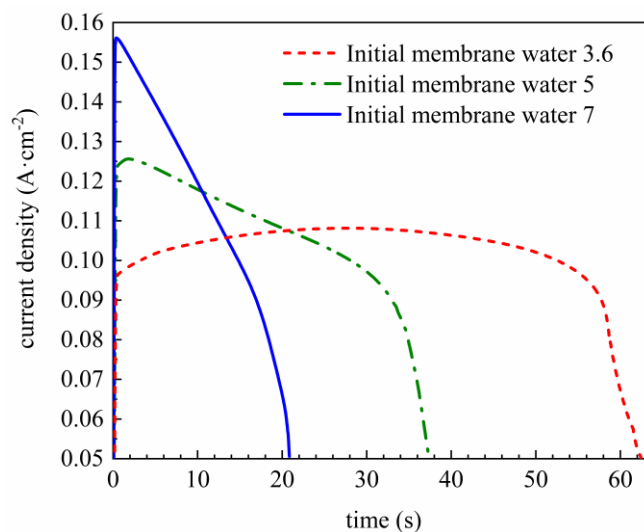


Fig. 3 Evolution of output current density of PEMFC during the cold start processes of different initial membrane water content

C. Effect Of Initial Membrane Water Content On Ice Volume Fraction

Figure 4 illustrates the distribution of ice volume fraction in the middle cross-section of the cathode catalytic layer of the PEMFC during a cold start under different initial membrane state water contents. The left side represents the inlet of the gas flow channel, and the right side represents the outlet. The upper and lower sections depict the catalytic layer in the under-ridge region, while the center corresponds to the catalytic layer in the flow channel region. As the cold start commences, reaction gases at both the cathode and anode enter the gas flow channels. The water generated in the cathode catalytic layer is absorbed by the electrolyte and begins to freeze in the pores of the catalytic layer upon

reaching saturation in the cold environment. The figure reveals that the under-ridge regions on both sides of the runner are the first to freeze, exhibiting a higher ice volume fraction than that in the gas runner region at the same moment. This disparity is attributed to the sweeping effect of the gas flow in the runner region, which more effectively carries away water, preventing saturation. In contrast, the under-ridge area, less affected by the gas flow, allows water to accumulate and reach supersaturation more readily. The figure also indicates that the distribution of icing along the gas flow direction is uneven, with the ice volume fraction being relatively lower at the runner inlet and in the middle of the runner at the catalytic layer. By the end of the cold start, the ice volume fraction in the catalytic layer approaches 1, indicating that the pores are completely blocked by ice, causing the reaction to cease.

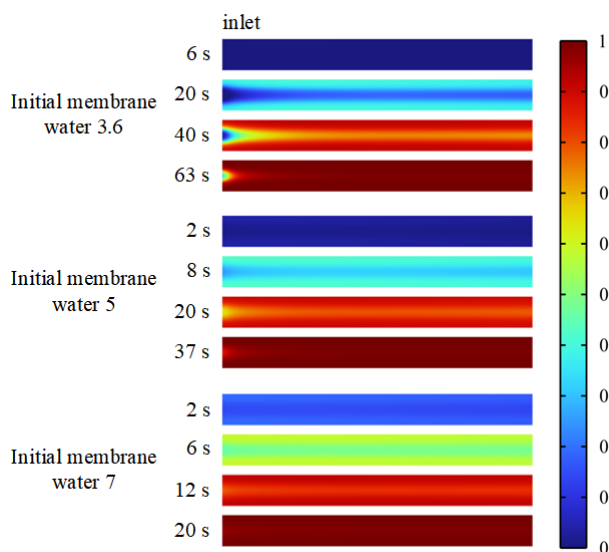


Fig. 4 Evolution of distribution of ice volume fraction in cathode CL during the cold start processes of different initial membrane water content

Figure 5 displays the change curves of the ice volume fraction in the cathode catalytic layer during the cold start of the fuel cell, comparing three different initial membrane state water contents. The data shows that when the initial membrane state water is 3.6, icing begins approximately 5 seconds after the cold start. Conversely, when the initial membrane state water content is 7, icing starts almost immediately upon initiating the cold start, indicating that lower initial water contents correspond to later icing times. This delay in icing is attributed to the lower initial water content in the electrolyte membrane, which offers a larger water storage space, thus enhancing the electrolyte's capacity to absorb water before reaching saturation. The graph also shows that lower initial water contents result in a slower icing rate. This slower rate can be linked to the dryer state of the proton exchange membrane, as shown in Figure 2. Lower water content leads to poorer conductivity, lower current density, reduced water production, and consequently, a slower rate of water phase transition to ice. As the ice volume fraction approaches 1, the cathode catalytic layer becomes blocked by ice, halting the electrochemical reaction and leading to cold start failure. Notably, the figure illustrates that with an initial membrane state water content of 3.6, compared to 7, the time to cold start failure is

extended by about 43 seconds.

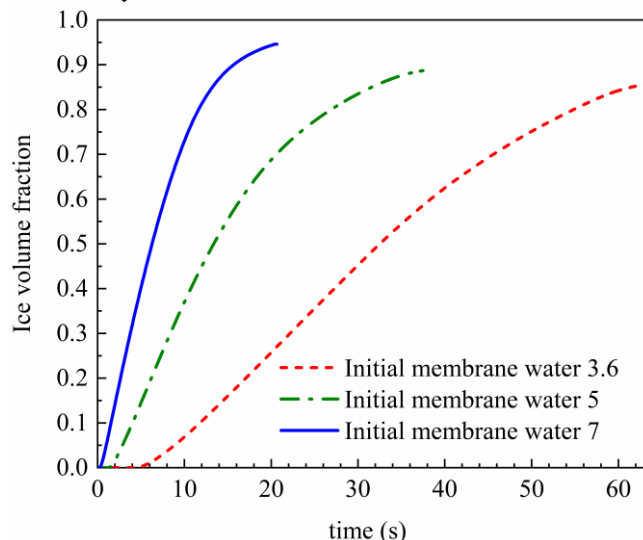


Fig. 5 Evolution of ice volume fraction in cathode CL during the cold-start processes of different initial membrane water content

D. Effect Of Initial Membrane Water Content On Temperature Change

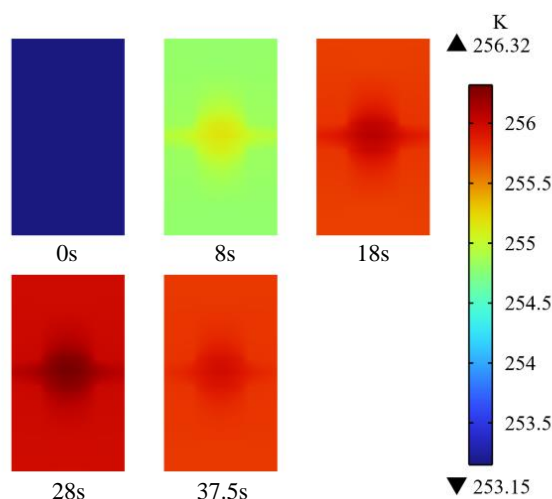


Fig. 6 Evolution of PEMFC temperature (K) during the cold-start process from -20°C with initial membrane water content at 5

Fig. 6 displays a cloud diagram showing the temperature distribution in the fuel cell at various moments during the cold start process, with an initial membrane state water content of 5. The diagram focuses on the longitudinal section at the middle position of the runner length direction. Within this section, the highest temperatures consistently occur in the center of the membrane electrode area corresponding to the runner. This central heating is due to the electrochemical reactions in the catalytic layer, which generate heat and subsequently raise the overall temperature of the cell. However, the temperature rise is initially uneven across the cell, gradually becoming more uniform as the overall temperature of the cell decreases later in the process. The most significant temperature increase is observed in the central membrane electrode area between the runners, where the concentration of reactive gases is highest. This results in a faster reaction rate, higher current density, and greater heat production in this area.

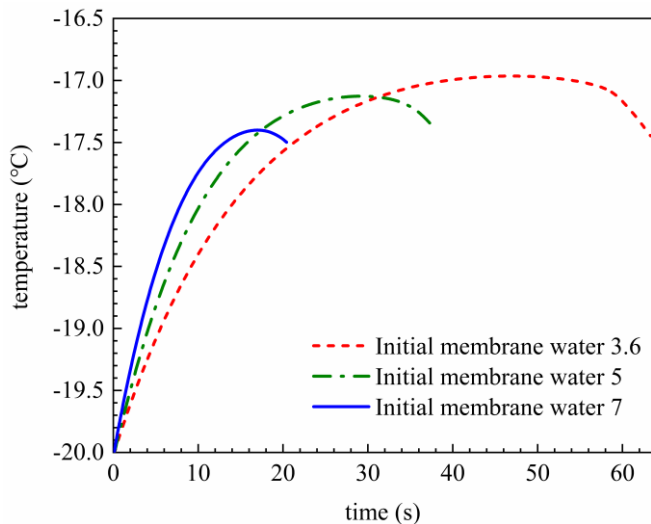


Fig. 7 Evolution of average temperature of PEMFC during the cold start processes of different initial membrane water content

Figure 7 illustrates the overall average temperature variations of the PEMFC during cold starts with different initial film states of water. The temperature trends for all cells initially rise to a maximum value and then begin to decrease. This decrease can be attributed to two main factors: first, the freezing of water in the cathode catalytic layer blocks pores, reducing the current density and consequently lowering heat production. Second, as the cell temperature exceeds the ambient temperature, heat dissipates into the external environment. When heat production falls below the rate of heat dissipation, the cell's temperature continues to decline. If the maximum cell temperature does not reach the freezing point, the produced water will continue converting to ice until the pores in the cathode catalyst layer are completely blocked, leading to a cold start failure. Additionally, Figure 7 indicates that higher initial film state water contents correspond to steeper temperature rise curves, suggesting quicker temperature increases. Conversely, lower initial water contents not only yield higher overall temperature increases but also extend the operational lifespan of the PEMFC during cold starts. For instance, with initial membrane water contents of 3.6 and initial membrane water contents of 7, the temperature rises are approximately 3.1 K and 2.6 K, respectively. Although all three cold-start scenarios ultimately fail and the temperature increases are modest, lower initial membrane water contents are more advantageous for prolonging the duration of the cold start and achieving higher temperature rises. Therefore, selecting a lower initial membrane water content is preferable to ensure normal operation during a cold start.

IV. CONCLUSION

In this paper, we established a three-dimensional multiphase flow multi-physics field coupled PEMFC cold start model and conducted transient simulations at a -20°C environment to study the impact of initial membrane state water content (3.6, 5, and 7) on cold start performance. The key findings of the study are:

1) Initial Film Water Content Influence: The initial film water content has a large impact on the output performance of the PEMFC at the onset of the cold start.

A lower initial water content leads to a smaller initial current density but allows for a longer period of smooth operation. Conversely, a higher initial water content results in a higher initial current density, which rapidly decays.

- 2) Icing Dynamics: Icing first appears at the cathode catalyst layer under the ridge during cold starts. As the initial film water content increases, icing initiates earlier within the cathode catalytic layer, the slope of the ice volume fraction curve steepens, and the icing accumulation rate accelerates, significantly reducing the cold-start operation time by up to 43 seconds. The distribution of icing within the cell is uneven, with lower ice volume fractions in the inlet and intermediate regions of the catalytic layer.
- 3) Temperature Dynamics and Distribution: The membrane electrode region corresponding to the gas flow channel heats up first, with the center region of the membrane electrode experiencing the most significant temperature rise. Cells with a low initial membrane water content produce more heat and a higher temperature rise than those with a high initial water content, thus enhancing the PEMFC's cold start capability by maintaining longer runtimes. The temperature distribution within the cell is uneven during the rise period but becomes more uniform as the temperature decreases.

REFERENCES

- [1] X. Xie, G. Zhang, J. Zhou, et al. Experimental and theoretical analysis of ionomer/carbon ratio effect on PEM fuel cell cold start operation, *Int. J. Hydrogen Energy* 42 (17) (2017) 12521–12530.
- [2] Y. Luo, K. Jiao, B. Jia, Elucidating the constant power, current and voltage cold start modes of proton exchange membrane fuel cell, *Int. J. Heat Mass Transf.* 77(2014) 489–500.
- [3] Lee C H, Tang J T. Modeling of the Ballard-Mark-V proton exchange membrane fuel cell with power converters for applications in autonomous underwater vehicles[J]. *Journal of Power Sources*. 2011, 196: 3810-3823.
- [4] Cui S T, Wang D L, Yan X Q, et al. Study on low temperature unassisted start-up of fuel cell stack (in Chinese). *Chin J Power Sources*, 2020, 44:1451–1455.
- [5] HE Pu, XIA Qiangfeng, JIANG Lixiang, et al. Effects of Pt Loading on the Cathode Catalyst Layer During the Cold Start Process[J/OL]. *Journal of Xi'an Jiaotong University*: 1-12[2023-09-26].
- [6] Zhao Jie, Li Wenhao, Du Changqing, et al. Numerical Simulation Study of Low Temperature Cold Start of PEMFC Under Different Operating and Environmental Conditions[J]. *Acta Energetica Solaris Sinica*, 2022, 43(06): 460-466.
- [7] Hosseini M, Afrouzi H H, Arasteh H, et al. Energy Analysis of a Proton Exchange Membrane Fuel Cell (PEMFC) with an Open-ended Anode Using Agglomerate Model: A CFD Study[J]. *Energy*, 2019, 188: 116090.
- [8] XU Peng, XU Sichuan, GUO Xin, et al. A Layered Numerical Model for Cold Start in Proton Exchange Membrane Fuel Cell[J]. *Journal of Tongji University (Natural Science)*, 2019, 47(01): 104-112.
- [9] YAO Lei, PENG Jie, ZHANG Jianbo, et al. Numerical simulation of cold start processes in proton exchange membrane fuel cell[J]. *Chemical Industry and Engineering Progress*, 2019, 38(09): 4029-4035.
- [10] Wei L, Dafalla A M, Jiang F M. Effects of reactants/coolant non-uniform inflow on the cold start performance of PEMFC stack[J]. *International Journal of Hydrogen Energy*, 2020, 45(24): 13469-13482.
- [11] LIAO Z, WEI L, DAFALLA A M, et al. Numerical study of subfreezing temperature cold start of proton exchange membrane fuel cells with zigzag-channeled flow field [J]. *Int J Heat Mass Tran*, 2021, 165: 120733.
- [12] Yang L, Cao C X, Gan Q Q, et al. Revealing failure modes and effect of catalyst layer properties for PEM fuel cell cold start using an agglomerate model[J]. *Applied Energy*, 2022, 312, 118792.

- [13] Ko J, Kim W, Hong T, et al. Impact of metallic bipolar plates on cold-start behaviors of Polymer electrolyte Fuel Cells (PEFCs)[J]. Solid State Ionics, Diffusion & Reactions, 2012, 225(none): 260-267.
- [14] Jiao K, Li X. Three-dimensional multiphase modeling of cold start processes in polymer electrolyte membrane fuel cells[J]. Electrochimica Acta, 2009, 54(27): 6876-6891.
- [15] Jiao K, Li X. Effects of various operating and initial conditions on cold start performance of polymer electrolyte membrane fuel cells[J]. International Journal of Hydrogen Energy, 2009, 34(19): 8171-8184.